Available online at www.sciencedirect.com
SCIENCE DIRECT®
PERGAMON
International Journal of Heat and Mass Transfer 46 (2003) 2887–2898
International Journal of HEAT and MASS TRANSFER
www.elsevier.com/locate/ijhmt

Global simulation of a silicon Czochralski furnace in an axial magnetic field

You-Rong Li [a,*], Deng-Fang Ruan [b], Nobuyuki Imaishi [c], Shuang-Ying Wu [a], Lan Peng [a], Dan-Ling Zeng [a]

[a] College of Power Engineering, Chongqing University, Chongqing 400044, China
[b] College of Mechanical Engineering, Chongqing University, Chongqing 400044, China
[c] Institute of Advanced Material Study, Kyushu University, 6-1 Kasuga-koen, Kasuga, Fukuoka 816-8580, Japan

Received 10 December 2002

Abstract

Control of melt flow in crystal growth process by application of the magnetic field is a practical technique for silicon single crystals. In order to understand the influence of axial magnetic field on the silicon melt flow and oxygen transport in a silicon Czochralski (Cz) furnace, a set of global numerical simulations was conducted using the finite-element method for the magnetic field strength from 0 to 0.3 T, the crystal rotation rates from 0 to 30 rpm and the crucible counter-rotation rates from 0 to −15 rpm. It was assumed that the flow was axisymmetric laminar in both the melt and the gas, the melt was incompressible and a constant temperature was imposed on the outer wall of the Cz furnace. The results indicate significantly different flow patterns, thermal and oxygen concentration fields in the melt pool when a uniform axial magnetic field is applied.

1. Introduction

The Czochralski (Cz) crystal growth is one of the most important methods of producing single crystal from the melt, in which the quality of single crystal depends mainly on the melt flow status. In the terrestrial environment, buoyancy and thermocapillary force are two major causes for melt convection. As the silicon melt is highly electrically conducting, application of magnetic field becomes a practical method to suppress flows induced by the buoyancy and thermocapillary force for the silicon crystal growth [1]. In this way, it is very important to have a clear understanding of the physical processes in a Cz furnace with variations of magnetic fields in order to produce high quality silicon crystal efficiently and economically. In recent years, many numerical simulations [2–10], experimental studies [4–6,11] and theoretical analyses [12,13] have been conducted on the melt flow and the oxygen transport in the silicon melt for the Cz furnace with the magnetic fields. But, in these numerical simulations, boundary condition for the heat transfer equation at the crucible wall was considered to be either a given temperature distribution [3,4,8,10] or a constant heat flux [2,9], and that at the melt/gas interface was approximated by a radiation heat loss to a constant ambient temperature [2,4,8]. Furthermore, boundary condition for the oxygen diffusion equation at the melt/gas interface was considered to be either a zero oxygen concentration [3,4] or a constant evaporation coefficient [5–7], which is in contrast to the experimental results obtained by Machida et al. [14]. Obviously, these reported numerical models could not adopt the real boundary conditions in a Cz furnace. In fact, in the Cz furnace crystal growth, heat transfer and oxygen mass transfer, as well as the flows in gas and melt phases are all closely related to each other. In order to understand the overall characteristics of a Cz furnace, it is necessary to apply a global numerical simulation which includes the whole heat exchange in the entire

* Corresponding author. Tel.: +86-23-6510-4834; fax: +86-23-6510-2473.
E-mail address: liyourong@yahoo.com (Y.-R. Li).

0017-9310/03/$ - see front matter © 2003 Elsevier Science Ltd. All rights reserved.
doi:10.1016/S0017-9310(03)00049-8

Nomenclature

A_i	the ith surface area
B	magnetic field strength
c	molar density
C_p	heat capacity
D	mass diffusivity
$\boldsymbol{e}$	unit vector
g	gravitational acceleration constant
G_{ji}	Gebhart's absorption factor
G_n	temperature gradient in the normal direction of the melt/crystal interface
ΔH_s	latent heat of fusion
$\boldsymbol{J}$	electric current
k	segregation coefficient
$\boldsymbol{n}$	unit normal vector of the interface element
n	rotation rate
P	pressure
$q_{\mathrm{rad},i}$	net radiative heat flux on the ith surface
Q	internal heat resource in the heater
$\boldsymbol{r}$	radius
$\boldsymbol{t}$	unit tangent vector of each interface element
T	temperature
u, v, w	the radial, axial and azimuthal components of velocity
$\boldsymbol{v}$	velocity vector
V_s	crystal pulling rate
x	molar fraction of oxygen in the melt
y	molar fraction of SiO in the gas phase

Greek symbols

β	thermal expansion coefficient
γ_T	surface tension temperature coefficient
ε	emissivity
λ	thermal conductivity
μ	dynamic viscosity
ρ	density
σ	electric conductivity
$\boldsymbol{\tau}$	stress tensor
Φ	electric scalar potential
ψ	stream function
Ω	angular rotation rate

Subscripts

c	crucible or center
f	furnace
g	gas
h	heater
l	melt
m	melting point
max	maximum
min	minimum
O	oxygen
s	crystal
z	axial direction
θ	azimuthal direction

furnace, melt and gas flows, and the transport of oxygen and SiO in the melt and in the gas, respectively. In our previous papers [15,16], the global numerical simulation for a small silicon Cz furnace was conducted, which clarified the significant influences of gas-phase transport phenomena, the Marangoni effect and the crystal and crucible rotations on the thermal environment, flow patterns, oxygen transport and oxygen concentrations on the melt/crystal interface. However, the application of magnetic field was neglected for the sake of simplicity. In this paper, the global numerical simulation was conducted to reveal the influence of the axial magnetic field on the silicon melt flow and oxygen transport.

2. Formulation of the problem

The configuration of the Cz furnace adopted in the present global numerical simulation is shown in Fig. 1. The inner diameter of crucible is 7.2 cm, and the diameter of crystal is 3.5 cm. A constant temperature T_0 ($=350$ K) is imposed on the outer wall of the Cz furnace. Argon gas flow rate is 0.5 L/min.

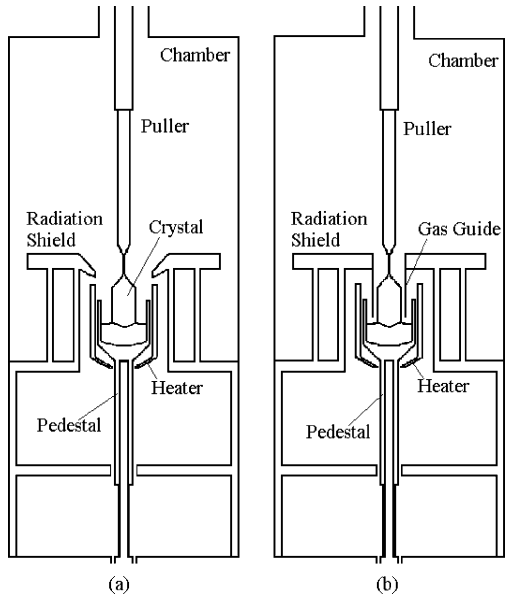

Fig. 1. The configuration of the Cz furnaces. (a) Without gas guide; (b) with gas guide.

The basic assumptions are introduced here as: (1) the flow is laminar in both the melt and the gas and the melt is incompressible Newtonian fluid satisfying the Boussinesq approximation except for the surface tension; (2) *P–V–T* relation of argon gas is expressed by the ideal gas law; (3) no supercooling occurs at the melt/crystal interface and the interface shape coincides with the melting temperature isotherm; (4) the oxygen concentration and the partial pressure of SiO are in chemical equilibrium at the melt–gas interface [17]; (5) the evaporated SiO does not deposit on any solid surface; (6) the melt and the crystal are considered to be surrounded by insulators at all boundaries, therefore the electric current is taken to be zero. Then, the governing equations for flow, temperature and concentration fields can be given as follows: In the melt

$$\nabla \cdot \boldsymbol{v}_\mathrm{l} = 0, \tag{1}$$

$$\rho_\mathrm{l} \boldsymbol{v}_\mathrm{l} \cdot \nabla \boldsymbol{v}_\mathrm{l} = -\nabla p_\mathrm{l} - \nabla \cdot \boldsymbol{\tau}_\mathrm{l} + \rho_\mathrm{l} g \beta (T_\mathrm{l} - T_\mathrm{m}) \boldsymbol{e}_z + \boldsymbol{F}_\mathrm{l}, \tag{2}$$

$$\rho_\mathrm{l} C_\mathrm{pl} \boldsymbol{v}_\mathrm{l} \cdot \nabla T_\mathrm{l} = \lambda_\mathrm{l} \nabla \cdot \nabla T_\mathrm{l}, \tag{3}$$

$$\boldsymbol{v}_\mathrm{l} \cdot \nabla x_\mathrm{O} = D_\mathrm{O} \nabla \cdot \nabla x_\mathrm{O}. \tag{4}$$

In the gas

$$\nabla \cdot (\rho_\mathrm{g} \boldsymbol{v}_\mathrm{g}) = 0, \tag{5}$$

$$\rho_\mathrm{g} \boldsymbol{v}_\mathrm{g} \cdot \nabla \boldsymbol{v}_\mathrm{g} = -\nabla p_\mathrm{g} - \nabla \cdot \boldsymbol{\tau}_\mathrm{g} - \rho_\mathrm{g} g \boldsymbol{e}_z, \tag{6}$$

$$\rho_\mathrm{g} C_\mathrm{pg} \boldsymbol{v}_\mathrm{g} \cdot \nabla T_\mathrm{g} = \nabla \cdot (\lambda_\mathrm{g} \nabla T_\mathrm{g}), \tag{7}$$

$$\nabla \cdot (C_\mathrm{g} \boldsymbol{v}_\mathrm{g} y_\mathrm{SiO}) = \nabla \cdot (C_\mathrm{g} D_\mathrm{SiO} \nabla y_\mathrm{SiO}). \tag{8}$$

In the crystal

$$\rho_\mathrm{s} C_\mathrm{ps} V_s \boldsymbol{e}_z \cdot \nabla T_\mathrm{s} = \nabla \cdot (\lambda_\mathrm{s} \nabla T_\mathrm{s}). \tag{9}$$

In the heater

$$\nabla \cdot (\lambda_\mathrm{h} \nabla T_\mathrm{h}) + Q = 0. \tag{10}$$

In the other solid materials

$$\nabla \cdot (\lambda_i \nabla T_i) = 0. \tag{11}$$

In Eq. (2), $\boldsymbol{F}_\mathrm{l}$ is the Lorentz force given by

$$\boldsymbol{F}_\mathrm{l} = \boldsymbol{J} \times B. \tag{12}$$

Taking into account Ohm's law and Kirchhoff's law,

$$\boldsymbol{J} = \sigma_\mathrm{l} (\boldsymbol{v}_\mathrm{l} \times B - \nabla \Phi), \tag{13}$$

$$\nabla \cdot \boldsymbol{J} = 0, \tag{14}$$

we can obtain the following equation for the electric scalar potential Φ:

$$\nabla^2 \Phi = \nabla (\boldsymbol{v}_\mathrm{l} \times B). \tag{15}$$

The Boundary conditions will be:

At the side wall and the bottom of the crucible

$$u_\mathrm{l} = 0, \quad v_\mathrm{l} = 0, \quad w_\mathrm{l} = r\Omega_\mathrm{c}, \tag{16a–c}$$

$$x_\mathrm{O} = 0.01 \times \mathrm{e}^{(7.8 - 22370/T)}, \tag{16d}$$

$$\boldsymbol{n} \cdot \boldsymbol{J} = 0. \tag{16e}$$

At the melt/gas interface

$$\boldsymbol{n} \cdot \boldsymbol{v}_\mathrm{l} = 0, \quad \boldsymbol{n} \cdot \boldsymbol{v}_\mathrm{g} = 0, \tag{17a–b}$$

$$\boldsymbol{\tau}_\mathrm{l} : \boldsymbol{nt} - \boldsymbol{\tau}_\mathrm{g} : \boldsymbol{nt} = \gamma_\mathrm{T} \nabla T_\mathrm{l} \cdot \boldsymbol{t}, \tag{17c}$$

$$\boldsymbol{t} \cdot v_\mathrm{l} - \boldsymbol{t} \cdot v_\mathrm{g} = 0, \tag{17d}$$

$$\boldsymbol{\tau}_\mathrm{l} : \boldsymbol{ne}_\theta - \boldsymbol{\tau}_\mathrm{g} : \boldsymbol{ne}_\theta = \gamma_\mathrm{T} \nabla T_\mathrm{l} \cdot \boldsymbol{e}_\theta, \tag{17e}$$

$$\boldsymbol{e}_\theta \cdot v_\mathrm{l} - \boldsymbol{e}_\theta \cdot \boldsymbol{v}_\mathrm{g} = 0, \tag{17f}$$

$$-\lambda_\mathrm{l} \boldsymbol{n} \cdot \nabla T_\mathrm{l} = -\lambda_\mathrm{g} \boldsymbol{n} \cdot \nabla T_\mathrm{g} + q_\mathrm{rad,l}, \tag{17g}$$

$$y_\mathrm{SiO} = 101325 x_\mathrm{O} \mathrm{e}^{(17.8 - 21000.0/T)} / P_0, \tag{17h}$$

$$-c_\mathrm{g} D_\mathrm{SiO} \boldsymbol{n} \cdot \nabla y_\mathrm{SiO} = -c_\mathrm{l} D_\mathrm{O} \boldsymbol{n} \cdot \nabla x_\mathrm{O}, \tag{17i}$$

$$\boldsymbol{n} \cdot \boldsymbol{J}_\mathrm{l} = 0. \tag{17j}$$

At the melt/crystal interface

$$u_\mathrm{l} = 0, \quad v_\mathrm{l} = 0, \quad w_\mathrm{l} = r\Omega_\mathrm{s}, \tag{18a–c}$$

$$\lambda_\mathrm{l} \boldsymbol{n} \cdot \nabla T_\mathrm{l} - \lambda_\mathrm{s} \boldsymbol{n} \cdot \nabla T_\mathrm{s} = \rho_\mathrm{s} V_s \Delta H_s \boldsymbol{n} \cdot \boldsymbol{e}_z, \tag{18d}$$

$$T_\mathrm{l} = T_\mathrm{s} = T_\mathrm{m}, \tag{18e}$$

$$\boldsymbol{n} \cdot \nabla x_\mathrm{O} = V_{s,n} (1 - k) x_\mathrm{O} / D_\mathrm{O}, \tag{18f}$$

$$\boldsymbol{n} \cdot \boldsymbol{J}_\mathrm{l} - \boldsymbol{n} \cdot \boldsymbol{J}_\mathrm{s} = 0. \tag{18g}$$

At the inlet of Ar gas

$$u_\mathrm{g} = w_\mathrm{g} = 0, \quad v_\mathrm{g} = v_\mathrm{in}, \tag{19a–c}$$

$$T_\mathrm{g} = T_\mathrm{g0}, \tag{19d}$$

$$y_\mathrm{SiO} = 0. \tag{19e}$$

At the outlet of gas

$$\boldsymbol{\tau} \cdot \boldsymbol{n} = 0, \tag{20a}$$

$$\boldsymbol{n} \cdot \nabla T_\mathrm{g} = 0, \tag{20b}$$

$$\frac{\partial y_\mathrm{SiO}}{\partial z} = 0. \tag{20c}$$

At the other exposed surfaces

$$-\lambda_i \boldsymbol{n} \cdot \nabla T_i = -\lambda_\mathrm{g} \boldsymbol{n} \cdot \nabla T_\mathrm{g} + q_\mathrm{rad,}i, \tag{21a}$$

$$\boldsymbol{n} \cdot \nabla y_\mathrm{SiO} = 0. \tag{21b}$$

At the other crucible surfaces and the pedestal surface

$$u_\mathrm{g} = v_\mathrm{g} = 0, \quad w_\mathrm{g} = r\Omega_\mathrm{c} \tag{22a–c}$$

At the other surfaces of crystal and the puller surface

$$u_\mathrm{g} = v_\mathrm{g} = 0, \quad w_\mathrm{g} = r\Omega_\mathrm{s} \tag{23a–c}$$

At other motionless solid surfaces

$$u_\mathrm{g} = v_\mathrm{g} = w_\mathrm{g} = 0 \tag{24a–c}$$

At the crystal side and top

$$\boldsymbol{n}\cdot\boldsymbol{J}_s = 0. \tag{25}$$

The melt/crystal interface shape is determined such that Eq. (18e) is satisfied, i.e., the interface coincides with the melting-point isotherm.

In above equations, $q_{\mathrm{rad},i}$ is given by

$$q_{\mathrm{rad},i} = \varepsilon_i\sigma_B\left[T_i^4 - \left(\sum_j A_j\varepsilon_j T_j^4 G_{ji}\right)\Big/ A_i \Big/ \varepsilon_i\right]. \tag{26}$$

G_{ji} and as the view factors between any two surface elements in the furnace are calculated using our code [18].

3. Numerical procedure and calculation conditions

To solve this problem, the Galerkin finite-element method is used. The total numbers of elements, nodal points and unknowns are 54542, 55107 and 242486, respectively. For mass transfer calculations, we use much finer elements, especially in the melt phase, with 177,973 elements, 179,170 nodal points and 179,381 unknown variables. The sizes of the minimum elements that are located at the corner of the melt/gas interface and the crucible wall in the melt are $\Delta r_{\min} = 0.125$ mm, $\Delta z_{\min} = 0.073$ mm for the flow, heat transfer and electric scalar potential analysis, and $\Delta r_{\min} = 2.60$ μm, $\Delta z_{\min} = 0.71$ μm for the oxygen transport analysis. We are confident that these meshes are adequate for predicting the velocity, temperature and oxygen concentration distribution. The other descriptions and validation of the numerical procedure can be found in Refs. [15,16].

In the present work, the diameter and length of the crystal and the heater power are given. The crystal pull rate is treated as one of the unknown variables, together with velocities, pressures, temperatures, the electric scalar potential and the melt/crystal interface coordinates, by simultaneously solving the set of nonlinear algebraic equations using the Newton–Raphson method. The code requires only a set of operating conditions as input data, such as gas flow rate, gas phase pressure, heater power, furnace chamber wall temperature, geometry of the furnace, diameter and length of the crystal, and total volume of silicon (melt and crystal). Typical conditions and the thermophysical properties used in this work are listed in Table 1. The temperature coefficient of surface tension is assumed to be -7×10^5 N/m K, which is taken from the recent experiments of Nogi [19].

4. Results and discussion

A series of simulations has been conducted under different magnetic field strength (0.0–0.3) T for crystal rotation rates from 0 to 30 rpm, the crucible counter-rotation rates from 0 to −15 rpm, the total pressure 10 Torr and the gas flow rate 0.5 L/min (L: 10^{-3} m^3 at 0.1 MPa and 273 K). The typical values of the simulations are listed in Table 2 for a conventional Cz furnace and in Table 3 for a Cz furnace with a gas guide. To make the comparison valid, the pull rate is rigorously maintained at around 1.1 mm/min for all the results by adjusting the heater power properly. The maximum error of the pulling rate is less than 0.08 mm/min.

In the silicon melt, the centrifugal forces produced by crystal and/or crucible rotation and the Lorentz forces by the axial magnetic field suppress the large natural convection along the crucible wall as well as the heat transfer rate from the crucible wall. Therefore, the temperature difference between crucible wall and crystal across melt/gas interface tends to increase. To grow a crystal with the same diameter under the same pulling rate, the heater power input must be increased slightly compared with that without the magnetic field and/or rotation cases (see Tables 2 and 3).

The flow in the gas phase will be discussed now. Fig. 2 shows the isotherms (left) in the Cz furnace and the stream function (right) in gas phase at $B = 0.1$ T, $n_s = 30$ rpm and $n_c = -10$ rpm. A large toroidal roll cell caused by the buoyancy occupies the upper chamber, and fresh gas flows down along the cold chamber wall. In the hot zone, the gas guide changes the temperature and flow fields. To compare Fig. 2 with that in Ref. [15], the overall flow patterns in the gas phase are almost the same as those without rotation and magnetic field. Rotations of crucible, pedestal, crystal and pulling rod, as well as the axial magnetic field give insignificant effect on the strong natural convection in the gas phase.

4.1. Hot zone in a conventional Cz furnace

Fig. 3 shows the contours of the stream function and the azimuthal velocity, the temperature and the oxygen concentration distributions in the melt, the contours of SiO and the gas flow vectors near the melt/crystal interface, and the isotherms in the crystal in a conventional Cz furnace. In Fig. 3a, the crystal and the crucible are all stationary, melt flow is driven by the buoyancy and the Lorentz force. There is only a large toroidal roll cell in the melt pool, which flows upward along the crucible and extends throughout most of the melt pool. Because of the suppression action of Lorentz force, the flow in the melt pool becomes weaker and the temperature goes up, oxygen concentration at the melt/crucible interface increases thereby. This high-oxygen-concentration melt near the melt/crucible interface is effectively carried to the area below the melt/crystal by the natural convection. Then, the oxygen concentration in the crystal becomes higher than that without the magnetic

Table 1
Physical properties and processing parameters

Thermal conductivity	
$\lambda = 22.0$ W/m K (crystal), $\lambda = 64.0$ W/mK (melt), $\lambda = 2.98$ W/m K (quartz)	
$\lambda = 60.0$ W/m K (graphite, heater, pedestal, radiation shield and gas guide)	
$\lambda = 59.0$ W/m K (puller)	
Viscosity	
$\mu = 7.0 \times 10^{-4}$ kg/ms (melt)	
Diffusivity	
$D_O = 5 \times 10^{-8}$ m^2/s, $D_{SiO} = 8.626 \times 10^{-6} \times T^{1.75}/P$ m^2/s	
Density	
$\rho = 2530.0$ kg/m^3 (melt), $\rho = PM/RT$ kg/m^3 (argon gas)	
Electrical conductivity	
$\sigma = 1.2 \times 10^6$ (S/m) (melt), $\sigma = 5.8 \times 10^4$ (S/m) (crystal)	
Thermal expansion coefficient of melt	
$\beta = 1.5 \times 10^{-4}$ K^{-1}	
Segregation coefficient of oxygen	
$k = 0.8$	
Surface tension and its temperature coefficient	
$\gamma = 0.735$ N/m, $\gamma_T = -7.0 \times 10^{-5}$ N/m K	
Heat of fusion	
$\Delta H_s = 1410$ J/kg	
Heat capacity	
$C_{pl} = 1000$ J/kg K, $C_{ps} = 1000$ J/kg K, $C_{pg} = 521.5$ J/kg K	
Melting temperature	1683.0 K
Furnace pressure	1333 Pa (10 Torr)
Argon gas flow rate	0.5 normal l/min
Chamber wall temperature	350.0 K
Crucible inner diameter	0.072 m
Crystal diameter	0.035 m
Crystal rotation rates	0–30 rpm
Crucible counter-rotation rates	0–15 rpm
Contact angle between melt and crystal	$\theta_c = 11°$
Emissivity	
$\varepsilon = 0.55$ (Crystal, Chamber wall), $\varepsilon = 0.318$ (Melt), $\varepsilon = 0.50$ (quartz)	
$\varepsilon = 0.9$ (graphite, heater, pedestal, radiation shield, gas guide and puller)	

field (see Fig. 4a). On the other hand, the increased temperature difference between crucible wall and crystal across melt/gas interface enhances the Marangoni effect, and radial surface flow is accelerated. Thus the oxygen concentration distribution along the melt/crystal and melt/gas interfaces becomes more uniform.

When the crucible rotates, the melt flow pattern shown in Fig. 3b is similar to that of Fig. 3a. But it is very different from that without the magnetic field (as reported in Ref. [16]), in which there is a strong annular column of upward flow under the stationary crystal. This slow crucible rotation rate induces rigid-body-like rotation in a large volume of the melt phase, thus the contours of the azimuthal velocity are almost vertical. The application of the axial magnetic field makes the melt flow pattern much simpler. At the same time, the strength of the melt flow decreases with increasing of the crucible rotation rate, but the oxygen concentration at the center of the melt/crystal interface and the average oxygen concentration (averaged over the whole area of the melt/crystal interface) are very insensitive to the crucible rotation rate (see Table 2).

When the crystal rotates (Fig. 3c), the rotating crystal exerts a shear force on the melt at the melt/crystal interface, which drives an azimuthal flow through viscous forces. The centrifugal force induced by rotation produces a stable radial outward flow beneath the outside part of the crystal, which pumps up the melt from the bottom of the crucible where the oxygen concentration is high. When the crystal rotation rate is low, the buoyancy and thermocapillary force cooperate to induce a strong convection cell in the melt phase. The surface flow penetrates under the melt/crystal interface to the center. The low oxygen concentration melt in the very thin layer under the melt surface is carried to the center by this strong surface flow. However, when the crystal rotation rate exceeds about 14 rpm, the upwelling flow of high oxygen concentration melt from the crucible bottom reaches the melt/crystal interface. The oxygen concentration on the melt/crystal interface becomes

Table 2
Summary of simulation results for a conventional Cz furnace

n_s (rpm)	n_c (rpm)	B (T)	Heater power (kW)	$T_{max,f}$ (K)	$T_{max,m}$ (K)	ΔT (K)	$[O]_{max}$ (atoms/cm^3)	$[O]_{min}$ (atoms/cm^3)	$[O]_{lc}$ (atoms/cm^3)		$y_{SiO,max}$	$\psi_{l,min}$ (cm^3/s)	$\psi_{l,max}$ (cm^3/s)	$v_{max,m}$ (cm/s)
									On the axis	Average				
0	0	0.1	17.43	1794.8	1705.9	21.16	2.68×10^{18}	6.54×10^{17}	7.37×10^{17}	7.06×10^{17}	0.884	−0.549	0	5.20
0	−2	0.1	17.43	1794.8	1705.9	21.16	2.68×10^{18}	6.53×10^{17}	7.34×10^{17}	7.05×10^{17}	0.884	−0.542	0	5.20
0	−6	0.1	17.43	1794.8	1705.9	21.12	2.68×10^{18}	6.53×10^{17}	7.36×10^{17}	7.05×10^{17}	0.883	−0.537	0	5.20
0	−10	0.1	17.44	1794.9	1705.9	21.05	2.68×10^{18}	6.50×10^{17}	7.33×10^{17}	7.02×10^{17}	0.882	−0.512	0	5.18
0	−15	0.1	17.45	1795.4	1706.2	21.02	2.69×10^{18}	6.48×10^{17}	7.31×10^{17}	7.00×10^{17}	0.882	−0.490	0	5.12
10	0	0.1	17.44	1795.2	1706.2	21.45	2.68×10^{18}	6.58×10^{17}	7.34×10^{17}	7.10×10^{17}	0.888	−0.547	0.003	5.26
20	0	0.1	17.52	1796.2	1707.1	22.35	2.70×10^{18}	6.76×10^{17}	1.39×10^{18}	1.16×10^{18}	0.900	−0.574	0.189	5.38
30	0	0.1	17.50	1797.0	1707.7	22.97	2.72×10^{18}	6.93×10^{17}	1.77×10^{18}	1.49×10^{18}	0.908	−0.625	0.370	5.39
10	−10	0.1	17.47	1795.8	1706.6	21.62	2.69×10^{18}	6.53×10^{17}	7.30×10^{17}	7.07×10^{17}	0.890	−0.509	0.027	5.19
20	−10	0.1	17.52	1797.5	1708.0	22.90	2.72×10^{18}	6.75×10^{17}	1.37×10^{18}	1.22×10^{18}	0.907	−0.502	0.267	5.27
30	−10	0.1	17.57	1799.0	1708.8	23.76	2.74×10^{18}	7.11×10^{17}	1.70×10^{18}	1.53×10^{18}	0.919	−0.389	0.489	4.74
20	−6	0.1	17.47	1798.2	1708.6	23.80	2.73×10^{18}	6.95×10^{17}	1.42×10^{18}	1.22×10^{18}	0.919	−0.524	0.291	5.16
20	−15	0.1	17.59	1799.6	1709.6	24.08	2.76×10^{18}	6.86×10^{17}	1.34×10^{18}	1.19×10^{18}	0.923	−0.253	0.262	4.79
20	−10	0.05	17.46	1795.5	1706.4	21.55	2.69×10^{18}	6.72×10^{17}	1.63×10^{18}	1.24×10^{18}	0.889	−0.698	0.280	5.63
20	−10	0.2	17.59	1799.8	1709.9	24.35	2.76×10^{18}	6.81×10^{17}	1.34×10^{18}	1.20×10^{18}	0.927	−0.279	0.208	4.33
20	−10	0.3	17.61	1800.2	1710.3	24.48	2.77×10^{18}	6.76×10^{17}	1.28×10^{18}	1.16×10^{18}	0.929	−0.252	0.171	3.96

Table 3
Summary of simulation results for a Cz furnace with a gas guide

n_s (rpm)	n_c (rpm)	B (T)	Heater power (kW)	$T_{max,f}$ (K)	$T_{max,m}$ (K)	ΔT (K)	$[O]_{max}$ (atoms/cm^3)	$[O]_{min}$ (atoms/cm^3)	$[O]_{lc}$ (atoms/cm^3)		$y_{SiO,max}$	$\psi_{l,min}$ (cm^3/s)	$\psi_{l,max}$ (cm^3/s)	$v_{max,m}$ (cm/s)
									On the axis	Average				
0	0	0.1	16.50	1768.9	1702.0	18.50	2.60×10^{18}	8.77×10^{15}	8.52×10^{16}	7.89×10^{16}	0.849	−0.409	0.015	3.81
0	−2	0.1	16.51	1768.9	1702.0	18.51	2.60×10^{18}	8.78×10^{15}	8.52×10^{16}	7.90×10^{16}	0.849	−0.409	0.015	3.81
0	−6	0.1	16.50	1768.9	1702.0	18.46	2.60×10^{18}	8.88×10^{15}	8.58×10^{16}	7.96×10^{16}	0.849	−0.395	0.015	3.81
0	−10	0.1	15.51	1769.0	1702.0	18.41	2.60×10^{18}	9.17×10^{15}	8.83×10^{16}	8.19×10^{16}	0.848	−0.386	0.015	3.81
0	−15	0.1	16.51	1769.0	1702.0	18.31	2.60×10^{18}	9.84×10^{15}	9.48×10^{16}	8.79×10^{16}	0.847	−0.384	0.016	3.80
10	0	0.1	16.52	1769.3	1702.3	18.84	2.61×10^{18}	9.23×10^{15}	8.78×10^{16}	8.23×10^{16}	0.854	−0.408	0.014	3.85
20	0	0.1	16.56	1770.6	1703.4	19.86	2.63×10^{18}	1.00×10^{16}	9.90×10^{17}	7.30×10^{17}	0.867	−0.411	0.228	3.86
30	0	0.1	16.57	1771.1	1703.7	20.19	2.64×10^{18}	1.04×10^{16}	1.45×10^{18}	1.16×10^{18}	0.871	−0.422	0.400	3.64
20	−6	0.1	16.55	1770.5	1703.3	19.78	2.63×10^{18}	1.02×10^{16}	1.10×10^{18}	8.10×10^{17}	0.866	−0.407	0.214	3.86
20	−10	0.1	16.56	1770.5	1703.4	19.75	2.63×10^{18}	1.05×10^{16}	1.12×10^{18}	8.31×10^{17}	0.865	−0.397	0.219	3.85
20	−15	0.1	16.57	1771.0	1703.6	19.77	2.63×10^{18}	1.07×10^{16}	1.07×10^{18}	8.05×10^{17}	0.866	−0.358	0.251	3.77
10	−10	0.1	16.53	1769.6	1702.5	18.81	2.61×10^{18}	9.37×10^{15}	3.97×10^{17}	1.53×10^{17}	0.853	−0.386	0.031	3.83
30	−10	0.1	16.58	1771.4	1703.8	20.06	2.64×10^{18}	1.02×10^{16}	1.41×10^{18}	1.17×10^{18}	0.869	−0.382	0.450	3.28
20	−10	0.05	16.53	1770.6	1703.3	19.65	2.63×10^{18}	9.45×10^{15}	1.38×10^{18}	8.99×10^{17}	0.864	−0.396	0.261	3.99
20	−10	0.2	16.59	1771.7	1704.2	20.23	2.64×10^{18}	1.06×10^{16}	1.03×10^{18}	8.29×10^{17}	0.871	−0.199	0.188	3.42
30	−10	0.3	16.60	1771.9	1704.3	20.26	2.65×10^{18}	1.10×10^{16}	1.01×10^{18}	8.34×10^{17}	0.872	−0.132	0.144	3.12

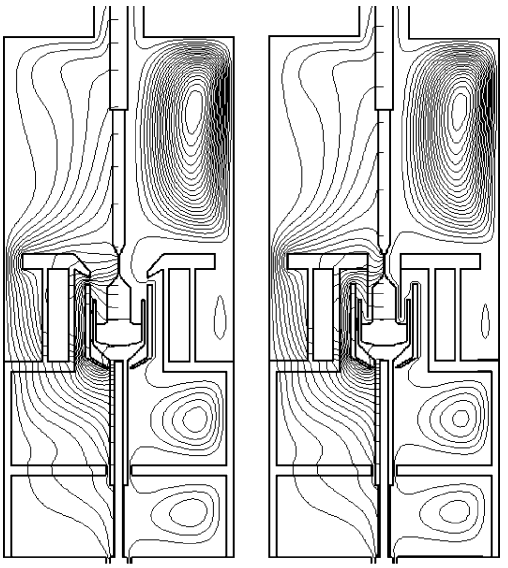

Fig. 2. Isotherms over the global furnace (left) and the stream functions in the gas phase (right). $\Delta T = 70$ K, $\Delta\psi = 0.0001$ m^3/s, $\psi_{max} = 0.00196$ m^3/s, $\psi_{min} = -0.000110$ m^3/s. (a) Without gas guide. (b) With gas guide.

high, slightly decreasing in the radial direction, as shown in Fig. 4b. This decrease is caused by mixing with the melt that is flowing inward along the surface and desorbs oxygen into gas phase. The melt of the outward flow driven by the crystal rotation beneath the crystal is mixed with that of the inward flow by the natural convection along the melt surface and ascends near the periphery of the crystal; therefore, there appears a strong annular column of downward flow. Furthermore, another weaker counter-clock flow cell is formed under the crystal of $r < r_s/2$, which causes another cold plume of downward flow along the axis and an annular column of upward flow at around $r = r_s/2$. This complex flow makes the oxygen concentration distribution become more uniform in the area near the center of the melt/crystal interface.

Under the combined crystal and crucible rotation, the melt flow pattern shown in Fig. 3d is similar to that of Fig. 3c. The crucible rotation makes the natural convective roll cell under the melt surface weaken and the melt flow under the crystal enhance (see Table 2). The enhanced melt flow under the crystal produces the more uniform oxygen concentration on the melt/crystal interface, as shown in Fig. 4c.

The strength of the magnetic field has significant effect on the melt flow pattern and the oxygen transport, as shown in Fig. 3e and f. With the increasing of the strength of the magnetic field, the counter-clockwise roll cell driven by the buoyancy and clockwise that by the crystal rotation are all suppressed, the stream functions corresponding to these two cells reduce, as shown in Fig. 5a. However, the counter-clock flow cell under the area near the crystal center is enhanced. Then, the oxygen concentration distribution on the melt/crystal interface becomes uniform and low because of the decreasing high concentration melt flow upwelling near $r = r_s/2$ and the enhancing flow downward near the axis (see Fig. 5b). Fig. 5c summarizes the variation of the oxygen concentration at the center of the crystal and average oxygen concentration on the melt/crystal interface as a function of the magnetic field strength. These results suggest that, in a small conventional Cz furnace, the oxygen concentration in the crystal decreases monotonically with the magnetic field strength.

The melt convection pattern also plays an important role in the shape of the melt/crystal interface and the radial distribution of the term $(V_{s,n}/G_n)$ at the melt/crystal interface. Fig. 5d shows the radial distribution of $(V_{s,n}/G_n)$ for the conventional Cz furnace at the different magnetic field strength. Obviously, the values of $(V_{s,n}/G_n)$ show its maximum at the axis and monotonically decreases toward the crystal periphery. These results predict that, in this small Cz furnace, the vacancy and the intrinsic type point defects are dominant in the inner and the outer region of the crystal, respectively, which is the same as the results without the magnetic field [16].

4.2. Hot zone with a gas guide

Fig. 6 shows the contours of the stream function and the azimuthal velocity, the temperature and the oxygen concentration distributions in the melt, the contours of SiO and the gas flow vectors near the melt/crystal interface, and the isotherms in the crystal in a Cz furnace with a gas guide. At the same gas flow rate, installing a cylindrical gas guide decreases the heater power. At the same time, the maximum temperature at the melt/crucible interface as well as the maximum oxygen concentration are both decreased (compared Table 3 with Table 2). Besides these thermal effects, the gas guide exerts significant effects on the melt flow pattern and the oxygen mass transfer, as shown in Fig. 6a. The gas guide directs all of the gas to the melt surface. By flowing along the melt surface, gas induces shear stress in the melt. There appears a clockwise roll cell with low oxygen concentration in a restricted area below the gas guide, where the shear stress from gas flow becomes the largest. In this case, the low-oxygen-concentration melt collected in the shear-driven circulating flow zone is efficiently conveyed to the area beneath the melt/crystal interface by the Marangoni-driven inward surface flow through a very thin layer near the crystal. Therefore the oxygen

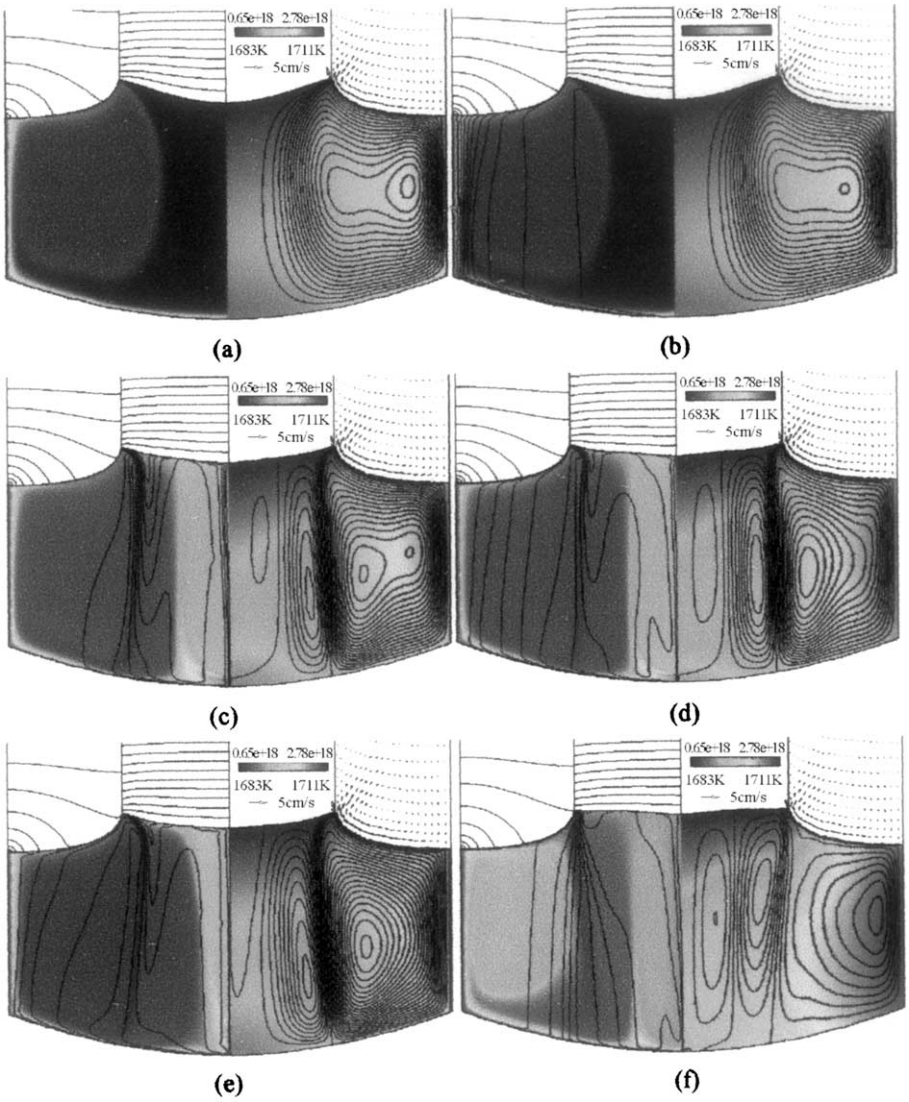

Fig. 3. Contours of stream function, ψ, and azimuthal velocity, w, temperature (T, color sacle on the right) and oxygen concentration (x_O, color scale on the left) in the melt, the contours of y_{SiO} and the gas flow vectors above the melt/gas interface, and the isotherms T_s in the crystal for a conventional Cz furnace, $\Delta\psi = 0.03 \times 10^{-6}$ m^3/s, $\Delta w = (w(+) - w(-))/10$, $\Delta y_{SiO} = 0.02$, $\Delta T_s = 5$ K. (a) $n_s = 0$, $n_c = 0$, $B = 0.1$ T, $\psi_{max} = 0$, $\psi_{min} = -0.549 \times 10^{-6}$ m^3/s, $y_{SiO,max} = 0.884$. (b) $n_s = 0$, $n_c = -10$ rpm, $B = 0.1$ T, $\psi_{max} = 0$, $\psi_{min} = -0.512 \times 10^{-6}$ m^3/s, $y_{SiO,max} = 0.882$, $w(+) = 0.19$ cm/s, $w(-) = -3.77$ cm/s. (c) $n_s = 20$ rpm, $n_c = 0$, $B = 0.1$ T, $\psi_{max} = 0.189 \times 10^{-6}$ m^3/s, $\psi_{min} = -0.574 \times 10^{-6}$ m^3/s, $y_{SiO,max} = 0.900$, $w(+) = 3.30$ cm/s, $w(-) = -0.18$ cm/s. (d) $n_s = 20$ rpm, $n_c = -10$ rpm, $B = 0.1$ T, $\psi_{max} = 0.267 \times 10^{-6}$ m^3/s, $\psi_{min} = -0.502 \times 10^{-6}$ m^3/s, $y_{SiO,max} = 0.907$, $w(+) = 3.35$ cm/s, $w(-) = -3.77$ cm/s. (e) $n_s = 20$ rpm, $n_c = -10$ rpm, $B = 0.05$ T, $\psi_{max} = 0.280 \times 10^{-6}$ m^3/s, $\psi_{min} = -0.698 \times 10^{-6}$ m^3/s, $y_{SiO,max} = 0.889$, $w(+) = 3.08$ cm/s, $w(-) = -3.77$ cm/s. (f) $n_s = 20$ rpm, $n_c = -10$ rpm, $B = 0.3$ T, $\psi_{max} = 0.171 \times 10^{-6}$ m^3/s, $\psi_{min} = -0.252 \times 10^{-6}$ m^3/s, $y_{SiO,max} = 0.929$, $w(+) = 3.61$ cm/s, $w(-) = -3.77$ cm/s.

concentration on the melt/crystal interface is very low. But compared with the results without the magnetic field (see Fig. 7 in Ref. [16]), it is found that the melt pool with low oxygen concentration becomes small and the oxygen concentration on the melt/crystal interface increases slightly, as shown in Fig. 7a.

When the crucible rotates, the melt flow pattern shown in Fig. 6b and the oxygen concentration distribution are similar to those without the crucible rotation. In this case, the natural convection roll cell prevails almost throughout the melt pool, and the strength of the melt flow decreases with increasing of the crucible

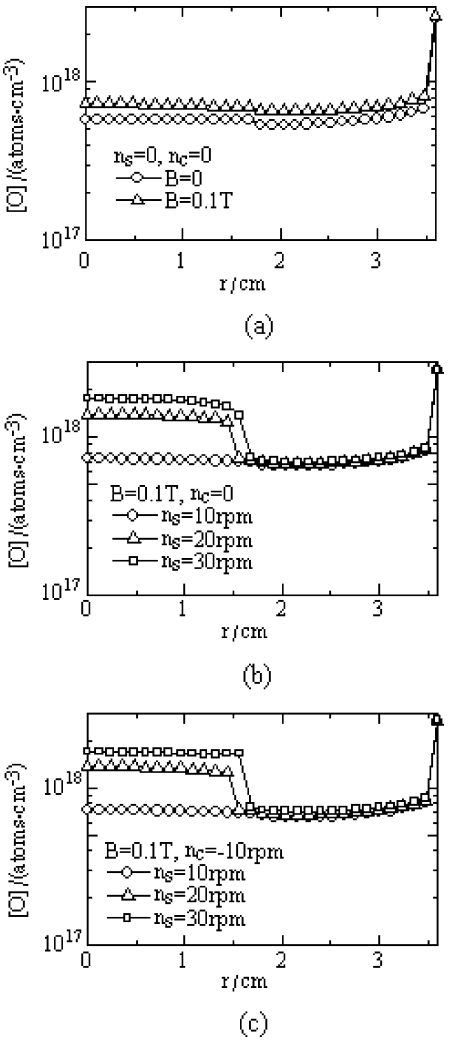

Fig. 4. Radial distributions of oxygen concentration at interfaces. (a) Without rotation. (b) Crystal rotation. (c) Combined crystal and crucible rotation.

rotation rate (see Table 3). When the crystal rotates, as pointed out in the previous part, there is an annular column of upward flow near $r = r_s/2$, which pumps up the melt from the bottom of the crucible where the oxygen concentration is high, as shown in Fig. 6c. Therefore the oxygen concentration on the melt/crystal interface becomes high. But when the crystal rotation is slower, such as $n_s = 10$ rpm, the pump-effect becomes weaker. The upwelling flow does not reach the melt/crystal interface. The oxygen concentration level at the melt/crystal interface is lower than that of $n_s = 20$ rpm, as shown in Fig. 7b.

Under the combined crystal and crucible rotation, the predicted results are shown in Fig. 6d under $n_s = 20$ rpm and $n_c = -10$ rpm. In this case, the magnetic field combined with the gas shear makes the flow pattern

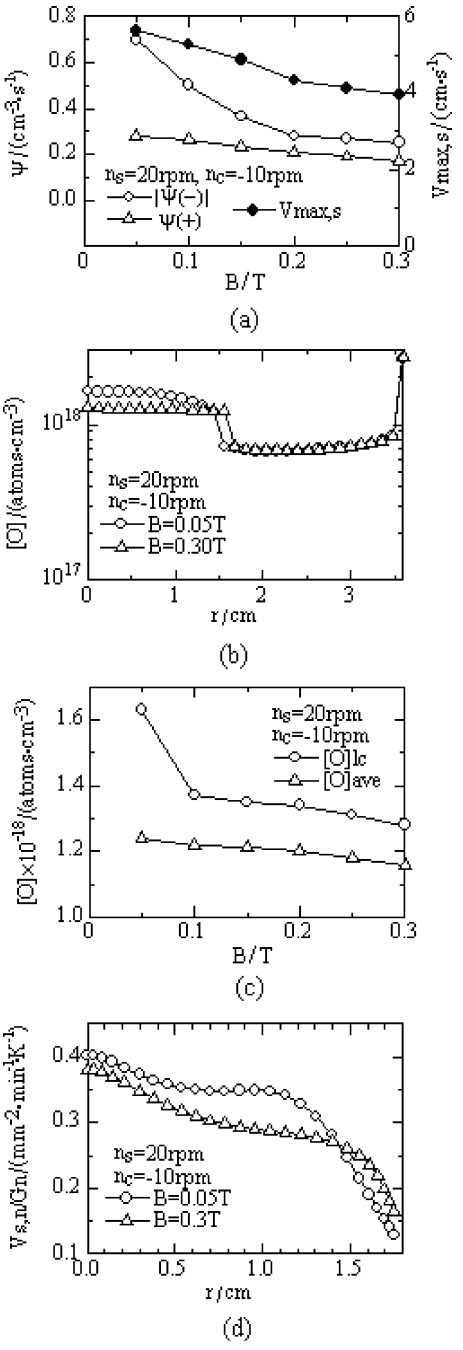

Fig. 5. Effect of the axial magnetic field at $n_s = 20$ rpm and $n_c = -10$ rpm. (a) Stream functions and the maximum surface velocity. (b) Radial distributions of oxygen concentration at interfaces. (c) The oxygen concentration at the center of the melt/crystal interface and the average oxygen concentration (averaged over the whole area of the melt/crystal interface). (d) Radial distributions of $(V_{s,n}/G_n)$ [mm^2/(min. K)] on the melt/crystal interface.

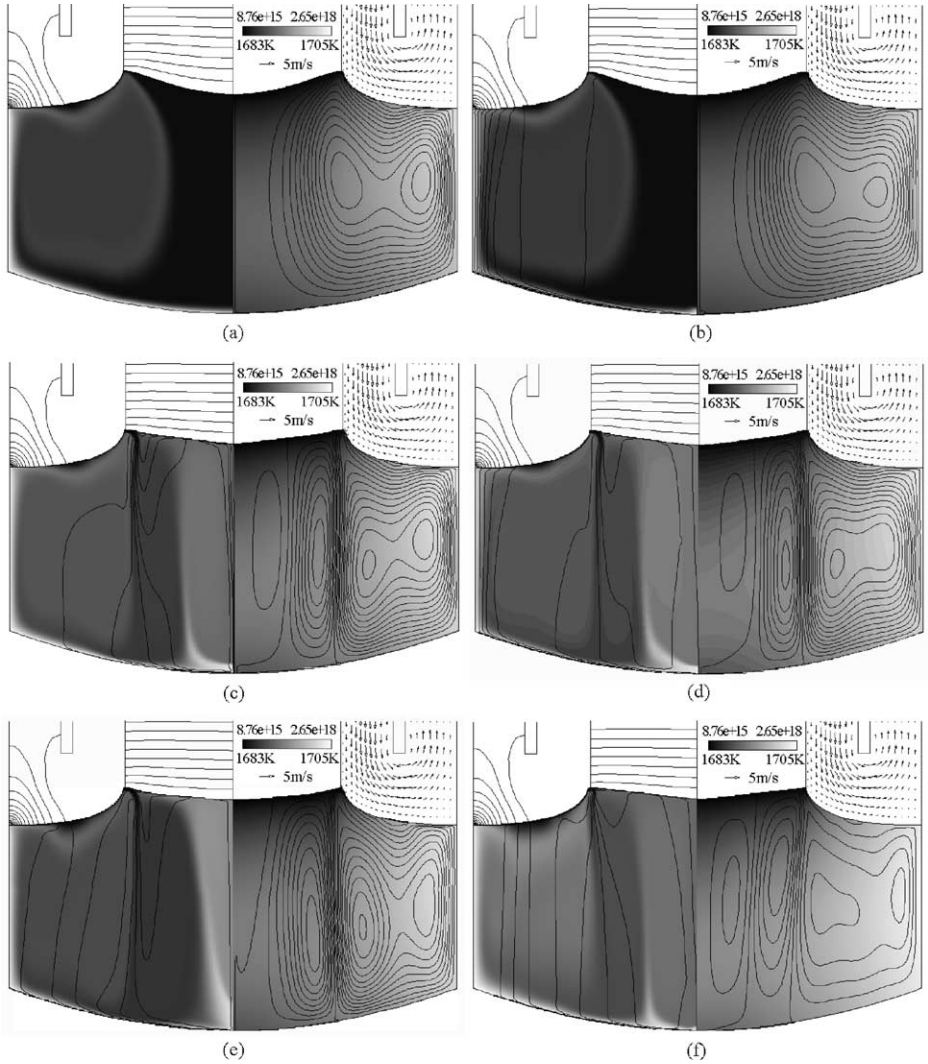

Fig. 6. Contours of stream function, ψ, and azimuthal velocity, w, temperature (T, on color scale the right) and oxygen concentration (x_O, color scale on the left) in the melt, the contours of y_{SiO} and the gas flow vectors above the melt/gas interface, and the isotherms T_s in the crystal for a Cz furnace with a gas guide, $\Delta\psi = 0.03 \times 10^{-6}$ m^3/s, $\Delta w = (w(+) - w(-))/10$, $\Delta y_{SiO} = 0.02$, $\Delta T_s = 5$ K. (a) $n_s = 0$, $n_c = 0$, $B = 0.1$ T, $\psi_{max} = 0.015 \times 10^{-6}$ m^3/s, $\psi_{min} = -0.409 \times 10^{-6}$ m^3/s, $y_{SiO,max} = 0.849$. (b) $n_s = 0$, $n_c = -10$ rpm, $B = 0.1$ T, $\psi_{max} = 0.015 \times 10^{-6}$ m^3/s, $\psi_{min} = -0.386 \times 10^{-6}$ m^3/s, $y_{SiO,max} = 0.848$, $w(+) = 0.23$ cm/s, $w(-) = -3.73$ cm/s. (c) $n_s = 20$ rpm, $n_c = 0$, $B = 0.1$ T, $\psi_{max} = 0.228 \times 10^{-6}$ m^3/s, $\psi_{min} = -0.411 \times 10^{-6}$ m^3/s, $y_{SiO,max} = 0.867$, $w(+) = 3.02$ cm/s, $w(-) = -0.39$ cm/s. (d) $n_s = 20$ rpm, $n_c = -10$ rpm, $B = 0.1$ T, $\psi_{max} = 0.219 \times 10^{-6}$ m^3/s, $\psi_{min} = -0.397 \times 10^{-6}$ m^3/s, $y_{SiO,max} = 0.865$, $w(+) = 3.02$ cm/s, $w(-) = -3.72$ cm/s. (e) $n_s = 20$ rpm, $n_c = -10$ rpm, $B = 0.05$ T, $\psi_{max} = 0.261 \times 10^{-6}$ m^3/s, $\psi_{min} = -0.396 \times 10^{-6}$ m^3/s, $y_{SiO,max} = 0.864$, $w(+) = 2.93$ cm/s, $w(-) = -3.76$ cm/s. (f) $n_s = 20$ rpm, $n_c = -10$ rpm, $B = 0.3$ T, $\psi_{max} = 0.144 \times 10^{-6}$ m^3/s, $\psi_{min} = -0.132 \times 10^{-6}$ m^3/s, $y_{SiO,max} = 0.872$, $w(+) = 3.04$ cm/s, $w(-) = -3.77$ cm/s.

more complex. The intensity of the upwelling flow near $r = r_s/2$ and the oxygen concentration distribution on the melt/crystal interface are very sensitive to the both rotation rates of crystal and crucible. For example, when $n_s = 10$ rpm and $n_c = -10$ rpm, thermocapillary flow conveys the low oxygen concentration melt to beneath the crystal, and this low oxygen melt is mixed with the high oxygen melt pumped up from the crucible bottom. Therefore, the oxygen concentration distribution on the melt/crystal interface exhibits a steep change near $r = r_s/2$, as shown in Fig. 7c.

Fig. 6e and f give the results of the melt flow pattern and the oxygen transport at $B = 0.05$ and 0.3 T, respectively. Obviously, the effect of magnetic field strength on the melt flow pattern and the oxygen transport in the Cz furnace with a gas guide is similar

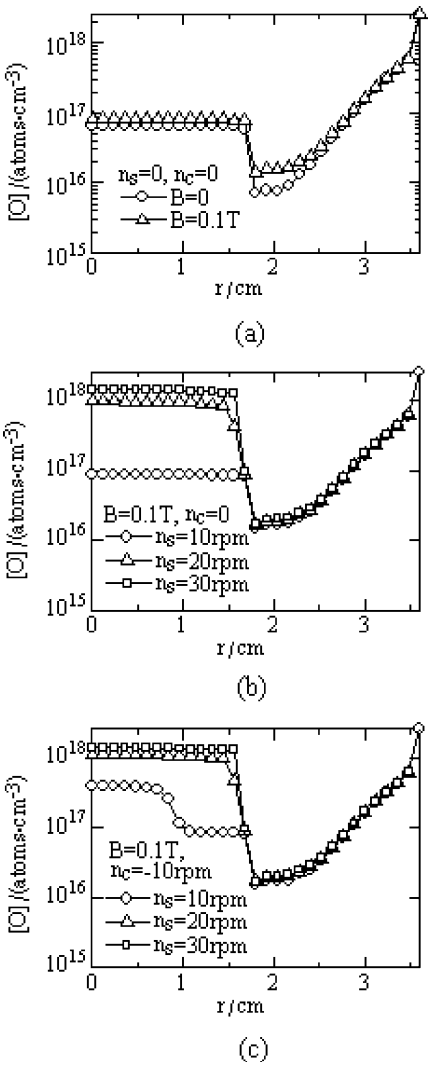

Fig. 7. Radial distributions of oxygen concentration at interfaces. (a) Without rotation. (b) Crystal rotation. (c) Combined crystal and crucible rotation.

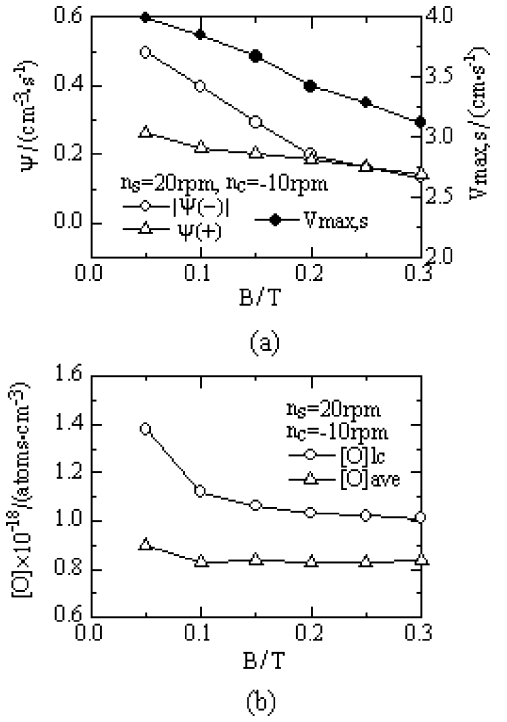

Fig. 8. Effect of the axial magnetic field at $n_s = 20$ rpm and $n_c = -10$ rpm. (a) Stream functions and the maximum surface velocity. (b) The oxygen concentration at the center of the melt/crystal interface and the average oxygen concentration (averaged over the whole area of the melt/crystal interface).

with that in a conventional Cz furnace. The variations of the maximum and minimum stream functions, the maximum velocity at the melt/gas interface, as well as the oxygen concentration at the center of the crystal and average oxygen concentration on the melt/crystal interface as a function of the magnetic field strength are shown in Fig. 8a and b, respectively.

5. Conclusions

A set of global numerical simulations based on a simple, laminar, axisymmetric and pseudo-steady model of a small silicon Cz furnace was conducted to reveal the influence of the axial magnetic field. The results confirm that the axial magnetic field suppresses the natural convection driven by buoyancy, retards heat transfer, increases the temperature difference between the crucible wall and crystal, and requires an increase of heater power.

When there is only the crucible rotation, the magnetic field makes the melt flow pattern become much simpler. But when the crystal rotates, three convective flow roll cells, driven by the thermal instability, the crystal rotation and the buoyancy respectively, appear in the melt pool. The melt flows under the rotating crystal (Cochlane flow and the slow upward flow near $r = r_s/2$) play important roles to determine the shape of the melt/crystal interface and the radial distributions of oxygen concentration.

The present results are not directly applicable to large industrial Cz furnaces because of the assumptions of laminar, axisymmetric and pseudo-steady-states. Further developments of numerical codes, which can combine the three-dimensional time-dependent melt flow and the turbulent flow in the gas phase, are need to extend the global analyses to more realistic conditions.

References

[1] D.T.J. Hurle, R.W. Series, Use of a magnetic field in melt growth, Handbook of crystal growth, vol. 2, North-Holland, Amsterdam, 1994 (pp. 259–285).

[2] P. Sabhapathy, M.E. Salcudean, Numerical study of Czochralski growth of silicon in an axisymmetric magnetic field, J. Cryst. Growth 113 (1991) 164–180.

[3] N. Kobayashi, Oxygen transport under an axial magnetic field in Czochralski silicon growth, J. Cryst. Growth 108 (1991) 240–246.

[4] H. Hirata, K. Hoshikawa, Three-dimensional numerical analyses of the effects of a cusp magnetic field on the floes, oxygen transport and heat transfer in a Czochralski silicon melt, J. Cryst. Growth 125 (1992) 181–207.

[5] K. Kakimoto, M. Eguchi, H. Ozoe, Use of an inhomogeneous magnetic field for silicon crystal growth, J. Crys. Growth 180 (1997) 442–449.

[6] M. Watanabe, K.M. Yi, T. Hibiya, K. Kakimoto, Direct observation and numerical simulation of molten silicon flow during crystal growth under magnetic fields by X-ray radiography and large scale computation, Progr. Crys. Growth Characterization Mater. (1999) 215–238.

[7] K. Kakimoto, Oxygen distribution in silicon melt under inhomogeneous transverse magnetic fields, J. Cryst. Growth 230 (2001) 100–107.

[8] J.S. Kim, T.Y. Lee, Numerical study of the melt-thermal effect on a silicon crystal in Czochralski growth system, J. Cryst. Growth 209 (2000) 55–67.

[9] V. Galindo, G. Gerbeth, W. von Ammon, E. Tomzig, J. Virbulig, Crystal growth melt flow control by means of magnetic fields, Energy Convers. Manage. 43 (2002) 309–316.

[10] B.H. Dennis, G.S. Dulikravich, Magnetic field suppression of melt flow in crystal growth, Int. J. Heat Fluid Flow, 23 (2002) 269–277.

[11] L. Gorbunov, A. Klyukin, A. Pedchenko, A. Feodorov, Melt flow instability and vortex structures in Czochralski growth under steady magnetic fields, Energy Convers. Manage. 43 (2002) 317–326.

[12] L.N. Hjellming, J.S. Walker, Melt motion in a Czochralski crystal puller with an axial magnetic field: isothermal motion, J. Fluid Mech. 164 (1986) 237–273.

[13] L.N. Hjellming, A thermal model for Czochralski silicon crystal growth with an axial magnetic field, J. Cryst. Growth 104 (1990) 327–344.

[14] N. Machida, Y. Suzuki, K. Abe, N. Ono, M. Kida, Y. Shimizu, The effects of argon gas flow rate and furnace pressure on oxygen concentration in Czochralski-grown silicon crystals, J. Cryst. Growth 186 (1998) 362–368.

[15] M.W. Li, Y.R. Li, N. Imaishi, T. Tsukada, Global simulation of a silicon Czochralski furnace, J. Cryst. Growth 234 (2002) 32–46.

[16] Y.R. Li, Y. Akiyama, N. Imaishi, T. Tsukada, Global analysis of a small Czochralski furnace with rotating crystal and crucible, J. Cryst. Growth, submitted for publication.

[17] D.E. Bornside, R.A. Brown, T. Fujiwara, H. Fujiwara, T. Kubo, The effects of gas-phase convection carbon contamination of Czochralski-grown silicon, J. Electrochem. Soc. 142 (1995) 2790–2804.

[18] H. Honda, N. Imaishi, T. Tsukada, M. Hozawa, Effect of a funnel-shaped radiation shield on the characteristics of silicon CZ furnace, J. Chem. Eng. Jpn. 25 (1992) 84–89.

[19] K. Nogi, private communication.